Physics of near-wavelength high contrast gratings

Vadim Karagodsky and Connie J. Chang-Hasnain*

Department of Electrical Engineering and Computer Sciences, University of California, Berkeley, California 94720, USA

**cch@berkeley.edu*

Abstract: We present a simple theory explaining the extraordinary features of high-contrast optical gratings in the near-wavelength regime, particularly the very broadband high reflectivity (>99%) and the ultra-high quality factor resonances ($Q>10^7$). We present, for the first time, an intuitive explanation for both features using a simple phase selection rule, and reveal the anti-crossing and crossing effects between the grating modes. Our analytical results agree well with simulations and the experimental data obtained from vertical cavity surface emitting lasers incorporating a high contrast grating as top reflector.

©2012 Optical Society of America

OCIS codes: (050.2770) Gratings; (050.6624) Subwavelength structures; (260.2110) Electromagnetic optics.

References and links

1. E. G. Loewen and E. Popov, *Diffraction Gratings and Applications* (CRC Press, 1997).
2. B. C. Kress and P. Meyrueis, *Applied Digital Optics: from Micro-optics to Nanophotonics* (Wiley, 2009)
3. S. Astilean, P. Lalanne, P. Chavel, E. Cambril, and H. Launois, "High-efficiency subwavelength diffractive element patterned in a high-refractive-index material for 633 nm," Opt. Lett. **23**(7), 552–554 (1998).
4. S. Goeman, S. Boons, B. Dhoedt, K. Vandeputte, K. Caekebeke, P. Van Daele, and R. Baets, "First demonstration of highly reflective and highly polarization selective diffraction gratings (GIRO-gratings) for long-wavelength VCSELs," IEEE Photon. Technol. Lett. **10**(9), 1205–1207 (1998).
5. T. Glaser, S. Schröter, H. Bartelt, H.-J. Fuchs, and E.-B. Kley, "Diffractive optical isolator made of high-efficiency dielectric gratings only," Appl. Opt. **41**(18), 3558–3566 (2002).
6. D. Rosenblatt, A. Sharon, and A. A. Friesem, "Resonant grating waveguide structures," IEEE J. Quantum Electron. **33**(11), 2038–2059 (1997).
7. R. Magnusson and S. S. Wang, "New principle for optical filters," Appl. Phys. Lett. **61**(9), 1022–1024 (1992).
8. C. F. R. Mateus, M. C. Y. Huang, Y. Deng, A. R. Neureuther, and C. J. Chang-Hasnain, "Ultra-broadband mirror using low index cladded subwavelength grating," IEEE Photon. Technol. Lett. **16**(2), 518–520 (2004).
9. C. F. R. Mateus, M. C. Y. Huang, L. Chen, C. J. Chang-Hasnain, and Y. Suzuki, "Broad-band mirror (1.12-1.62 μm) using a subwavelength grating," IEEE Photon. Technol. Lett. **16**(7), 1676–1678 (2004).
10. Y. Zhou, M. C. Y. Huang, and C. J. Chang-Hasnain, "Large fabrication tolerance for VCSELs using high contrast grating," IEEE Photon. Technol. Lett. **20**(6), 434–436 (2008).
11. C. J. Chang-Hasnain, Y. Zhou, M. Huang, and C. Chase, "High-contrast grating VCSELs," IEEE J. Sel. Top. Quantum Electron. **15**(3), 869–878 (2009).
12. M. C. Y. Huang, Y. Zhou, and C. J. Chang-Hasnain, "A surface-emitting laser incorporating a high index-contrast subwavelength grating," Nat. Photonics **1**(2), 119–122 (2007).
13. M. C. Y. Huang, Y. Zhou, and C. J. Chang-Hasnain, "A nanoelectromechanical tunable laser," Nat. Photonics **2**(3), 180–184 (2008).
14. Y. Zhou, M. Moewe, J. Kern, M. C. Y. Huang, and C. J. Chang-Hasnain, "Surface-normal emission of a high-Q resonator using a subwavelength high-contrast grating," Opt. Express **16**(22), 17282–17287 (2008).
15. F. Brückner, D. Friedrich, T. Clausnitzer, M. Britzger, O. Burmeister, K. Danzmann, E. B. Kley, A. Tünnermann, and R. Schnabel, "Realization of a monolithic high-reflectivity cavity mirror from a single silicon crystal," Phys. Rev. Lett. **104**(16), 163903 (2010).
16. T. Stöferle, N. Moll, T. Wahlbrink, J. Bolten, T. Mollenhauer, U. Scherf, and R. F. Mahrt, "Ultracompact silicon/polymer laser with an absorption-insensitive nanophotonic resonator," Nano Lett. **10**(9), 3675–3678 (2010).
17. C. Sciancalepore, B. B. Bakir, X. Letartre, J. Harduin, N. Olivier, C. Seassal, J. Fedeli, and P. Viktorovitch, "CMOS-compatible ultra-compact 1.55- μ m emitting VCSELs using double photonic crystal mirrors," IEEE Photon. Technol. Lett. **24**(6), 455–457 (2012).

#160825 - $15.00 USD Received 4 Jan 2012; revised 12 Mar 2012; accepted 15 Apr 2012; published 26 Apr 2012
(C) 2012 OSA

18. Y. Zhou, V. Karagodsky, B. Pesala, F. G. Sedgwick, and C. J. Chang-Hasnain, "A novel ultra-low loss hollow-core waveguide using subwavelength high-contrast gratings," Opt. Express **17**(3), 1508–1517 (2009).
19. V. Karagodsky, B. Pesala, C. Chase, W. Hofmann, F. Koyama, and C. J. Chang-Hasnain, "Monolithically integrated multi-wavelength VCSEL arrays using high-contrast gratings," Opt. Express **18**(2), 694–699 (2010).
20. F. Lu, F. G. Sedgwick, V. Karagodsky, C. Chase, and C. J. Chang-Hasnain, "Planar high-numerical-aperture low-loss focusing reflectors and lenses using subwavelength high contrast gratings," Opt. Express **18**(12), 12606–12614 (2010).
21. D. Fattal, J. Li, Z. Peng, M. Fiorentino, and R. G. Beausoleil, "Flat dielectric grating reflectors with focusing abilities," Nat. Photonics **4**(7), 466–470 (2010).
22. B. Pesala, V. Karagodsky and C. Chang-Hasnain, ""Ultra-compact optical coupler and splitter using high-contrast grating hollow-core waveguide," in *Integrated Photonics Research, Silicon and Nanophotonics*, OSA Technical Digest (CD) (Optical Society of America, 2010), paper IWH1.
23. M. G. Moharam and T. K. Gaylord, "Rigorous coupled wave analysis of planar grating diffraction," J. Opt. Soc. Am. **71**(7), 811 (1981).
24. S. T. Peng, "Rigorous formulation of scattering and guidance by dielectric grating waveguides: general case of oblique incidence," J. Opt. Soc. Am. A **6**(12), 1869 (1989).
25. L. Li, "A modal analysis of lamellar diffraction gratings in conical mountings," J. Mod. Opt. **40**(4), 553–573 (1993).
26. P. Lalanne, J. P. Hugonin, and P. Chavel, "Optical properties of deep lamellar gratings: a coupled Bloch-mode insight," J. Lightwave Technol. **24**(6), 2442–2449 (2006).
27. V. Karagodsky, F. G. Sedgwick, and C. J. Chang-Hasnain, "Theoretical analysis of subwavelength high contrast grating reflectors," Opt. Express **18**(16), 16973–16988 (2010).
28. V. Karagodsky, C. Chase, and C. J. Chang-Hasnain, "Matrix Fabry-Perot resonance mechanism in high-contrast gratings," Opt. Lett. **36**(9), 1704–1706 (2011).
29. T. Tamir, G. Griffel, and H. L. Bertoni, eds., *Guided-Wave Optoelectronics*, 2nd ed. (Springer-Verlag, 1990).
30. C. Weisbuch, M. Nishioka, A. Ishikawa, and Y. Arakawa, "Observation of the coupled exciton-photon mode splitting in a semiconductor quantum microcavity," Phys. Rev. Lett. **69**(23), 3314–3317 (1992).
31. J. P. Reithmaier, G. Sęk, A. Löffler, C. Hofmann, S. Kuhn, S. Reitzenstein, L. V. Keldysh, V. D. Kulakovskii, T. L. Reinecke, and A. Forchel, "Strong coupling in a single quantum dot-semiconductor microcavity system," Nature **432**(7014), 197–200 (2004).
32. W. Shan, W. Walukiewicz, J. W. Ager III, E. E. Haller, J. F. Geisz, D. J. Friedman, J. M. Olson, and S. R. Kurtz, "Band anticrossing in GaInNAs alloy,s," Phys. Rev. Lett. **82**(6), 1221–1224 (1999).
33. D. J. Joannopoulos, S. G. Johnson, J. N. Winn, and R. D. Meade, *Photonic Crystals: Molding the Flow of Light*, 2nd ed. (Princeton University Press, 2008).
34. W. M. J. Green, M. J. Rooks, L. Sekaric, and Y. A. Vlasov, "Optical modulation using anti-crossing between paired amplitude and phase resonators," Opt. Express **15**(25), 17264–17272 (2007).

1. Introduction

Optical gratings are among the most fundamental building blocks in optics. They are well understood in two regimes: the diffraction regime, where the grating period (Λ) is greater than the wavelength (λ) [1] and the deep-subwavelength regime, where the grating period is much less than the wavelength [2]. However, between these two well-known regimes lies a third, relatively unexplored regime: the near-wavelength regime, here-in defined as a grating whose period is between the wavelengths inside the grating material and its surrounding media. For example, if a near-wavelength grating is made of material with index n_r and surrounded by n_a, its period would be between λ/n_r and λ/n_a. In this regime, gratings behave radically differently, and exhibit features that are not commonly attributed to gratings. With the advent of nanofabrication technologies, near-wavelength gratings have been explored for high reflectivity diffractive elements (85%–90%) [3,4], optical isolator [5], resonant grating waveguides as optical modulators or switches [6], and optical filters [7]. In all these cases, the gratings were typically etched into the substrate with a large index contrast with the medium on top, from which light incident. However, recently, we discovered a novel near-wavelength grating structure where the high index grating is *completely* surrounded by low index materials, referred as high-contrast gratings (HCG) [8]. By *fully* surrounding the high index medium with low index, many unexpected, extraordinary features that are uncommon to diffractive gratings were obtained. One of these features is broadband high reflectivity (>99%). Another feature is high quality-factor resonance ($Q>10^7$).

We reported an ultrabroadband, high reflectivity HCG with $\Delta\lambda/\lambda>30\%$ at >99% reflection [8]. The broadband mirror was experimentally verified [9] and implemented in vertical cavity

#160825 - $15.00 USD Received 4 Jan 2012; revised 12 Mar 2012; accepted 15 Apr 2012; published 26 Apr 2012
(C) 2012 OSA

surface emitting lasers (VCSELs) in place of conventional distributed Bragg reflectors (DBRs) [10–13]. The surface-normal high-Q resonance effect in a single-layer HCG was also proposed and verified [14]. Recently, Brückner et al. reported high reflectivity HCG mirror fabricated using an interesting T-shape grating to achieve index contrast with a single material [15]. Stöferle et al. realized a laser cavity using vertically standing HCGs, with emission in the direction parallel to the wafer surface [16]. In addition, Sciancalepore et al. Optically pumped VCSEL with top and bottom HCGs is achieved [17]. Additional promising applications of near-wavelength HCGs include hollow-core low-loss waveguides, whereby the light is guided between two grating mirrors [18], multi-wavelength VCSEL arrays [19], planar focusing reflectors [20,21], biosensors [14], ultra-compact optical couplers and splitters [22], etc.

To understand near-wavelength gratings, the electromagnetic field profile inside the grating can neither be approximated (as in the deep-subwavelength regime) nor ignored (as in the diffraction regime). Fully rigorous electromagnetic solutions exist for gratings [23–25], but they tend to involve heavy mathematical formulism. A quasi-analytical method using coupled Bloch modes was published with greatly simplified mathematics [26]. However, due to the inclusion of more general terms, they do not easily lead to simple physical intuition to explain the phenomena reported in Refs. [8–22]. Recently, we published a simple analytic formalism to explain the broadband reflection and resonance [27,28]. We showed that the resonances are due to coherent interference between two surface-normal waveguide array modes resulting from abrupt and large index contrast [28], whereas the broadband reflection is due to their destructive interference.

In this work, we present a very simple algorithm to tie the two seemingly opposite properties together. We discovered a simple phase selection rule, which for the first time completely trivializes HCG's extraordinary properties and leads to an intuitive design algorithm. Considering the wide range of optical applications, it is not difficult to appreciate the potential enormous scientific as well as technological impact of near-wavelength HCGs.

2. Theoretical frame work

Figure 1(a) describes the basic structure under consideration, consisting of dielectric gratings with a refractive index n_{bar} ($2<n_{bar}<3.5$), *completely* surrounded by a low index medium, e.g. air. The grating period, bar width, air gap and thickness are denoted by Λ, s, a, and t_g, respectively. As discussed in [27], the grating is assumed to be infinite in the y direction and infinitely periodic in the x direction. The incident light is assumed to be a plane wave propagating along the z direction. The grating bars can be considered as merely a periodic array of waveguides along z direction. Upon plane wave incidence, a few slab-waveguide-array modes are excited. These modes then depart from the grating input plane ($z = 0$) and propagate downward (+z direction) to the grating output plane ($z = t_g$), and then reflect back up. As mentioned, the extraordinary phenomena of near-wavelength gratings can be explained from the viewpoint of interference between these modes [27,28].

The two main types of phenomena observed in the subwavelength regime are shown in Fig. 1(b). The surface-normal reflectivity spectrum of *resonant gratings* (in red) exhibits several high-Q resonances, characterized by very sharp transitions from 0 to ~100% reflectivity, or vice versa. The reflectivity spectrum of *broadband grating reflectors* (in blue), exhibits reflectivity above 99% across a large bandwidth. The dispersion relation of the waveguide array modes for surface-normal incidence is given in [27] and repeated here for simple reference:

$$k_s \tan\left(k_s s/2\right) = -n_{bar}^2 k_a \tan\left(k_a a/2\right) \tag{1a}$$

$$\beta^2 = \left(2\pi/\lambda\right)^2 - k_a^2 = \left(2\pi n_{bar}/\lambda\right)^2 - k_s^2 \tag{1b}$$

#160825 - $15.00 USD Received 4 Jan 2012; revised 12 Mar 2012; accepted 15 Apr 2012; published 26 Apr 2012
(C) 2012 OSA

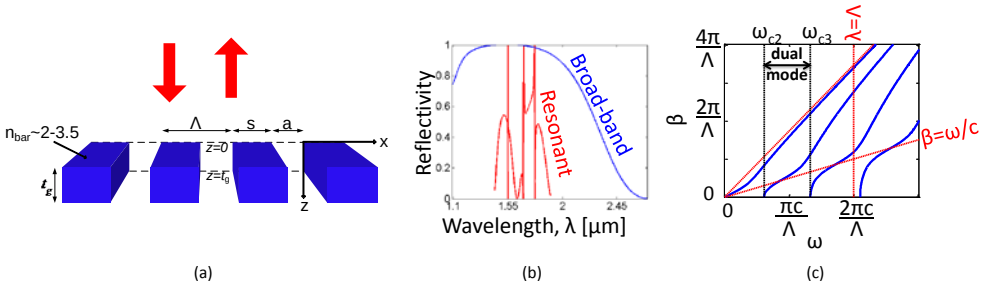

(a) (b) (c)

Fig. 1. (a) Basic HCG structure. The grating comprises of simple dielectric bars with high refractive index surrounded by a low index medium. The plane wave is incident from the top in the surface normal direction. The incident plane wave excites waveguide array modes, which propagate downward from $z = 0$ to $z = t_g$. (b) Examples of two types of extraordinary reflectivity features: broad-band high reflectivity (blue) and high-Q resonances (red). The broadband reflector HCG dimensions are: Λ = 772nm, t_g = 502nm, η = 77%, n_r = 3.2137 and TM polarized light. The high-Q resonator HCG is TE polarized with Λ = 716nm, t_g = 1494nm, η = 70%, n_r = 3.48. The spectra were calculated using RCWA. (c) Dispersion curves of the waveguide array modes (blue lines) calculated using analytic solutions: β being the z-wavenumbers. Between the two light lines (red, dashed) the dispersion resembles that of a slab waveguide [29]. However, below the air light line ($\beta<\omega/c$) there is a discrete set of modes due to subwavelength grating periodicity. ω_{c2} and ω_{c3} are the cutoffs of the second and the third modes respectively, and between them the grating operates at a dual-mode regime.

where β is the z-wavenumber (propagation constant) of the waveguide-array mode; and k_s and k_a are the x-wavenumbers inside the grating bars and inside air-gaps, respectively. The dispersion relation in Eq. (1) corresponds to E-field is along the x axis, referred as TM polarization of incidence. The dispersion relation for TE polarization of incidence (for which the E-field is along the y axis) is obtained by omitting the n_{bar}^2 factor in Eq. (1)(a) [27]. One may note the similarity of Eq. (1) with the characteristic equation of an ordinary slab waveguide [29]. To see Eq. (1) approaches to the characteristic equation of a slab waveguide, we can simply push period Λ and, hence, a to infinity. Equation (1)a cannot converge unless k_a is imaginary and, in which case, $\tan(k_a\, a/2) \rightarrow i$. Eq. 1a becomes exactly characteristic equation of a slab waveguide.

The ω-β relations ($\omega = 2\pi c/\lambda$) resulting from Eq. (1) are plotted in Fig. 1(c). First, we denote the light lines for air, $\beta = \omega/c$, and the dielectric $\beta = \omega n_{bar}/c$. The dispersion curves between the two light lines indeed resemble those of an ordinary slab waveguide [29]. Here, we see several trends which are the same to a slab waveguide: (1) as frequency increases, more and more modes exist; (2) except for the fundamental mode, there is a cut-off frequency (denoted by ω_{c2}, ω_{c3}, etc.) for each higher order mode (cutoff condition being $\beta = 0$); and (3) the higher the order of the mode, the higher the cut-off frequency (the shorter the cut-off wavelength).

One main difference from ordinary slab waveguides stands-out: HCG has a discrete set of modes below the air light line, i.e. $\beta<\omega/c$, in contrast to the continuum of radiation modes observed for a slab waveguide. This discretization is a direct consequence of the grating periodicity. The cutoff frequencies in Fig. 1(c) are important, since they determine the regime in which the grating operates. As will be shown subsequently, the extraordinary features discussed in the introduction are observed primarily in the regime where exactly two modes exist, hereinafter the "dual-mode" regime.

3. Phase selection rules of HCG

Figure 2(a) shows a simulated reflectivity contour map versus normalized wavelength and grating thickness (both by Λ) for a surface-normal incident TE-plane wave onto a HCG with $n_{bar} = 3.48$ and a duty cycle of $\eta = s/\Lambda = 0.7$ using rigorous coupled wave analysis (RCWA)

#160825 - $15.00 USD Received 4 Jan 2012; revised 12 Mar 2012; accepted 15 Apr 2012; published 26 Apr 2012
(C) 2012 OSA

[23]. A fascinatingly well-behaved, highly ordered, checker-board pattern reveals a strong dependence on both wavelength and HCG thickness, which indicates an interference effect. This checker-board pattern is particularly pronounced in the *dual-mode* regime for wavelengths between λ_{c2} and λ_{c3} (cut-off wavelengths of the second and third waveguide array modes, respectively). We further note that half of the "checker boxes" have high reflectivity (dark red contour), while the other half have lower reflectivity.

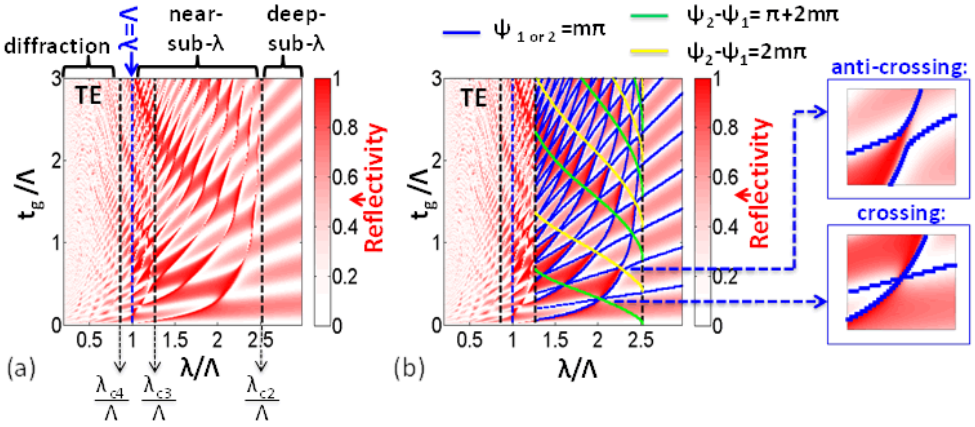

Fig. 2. (a) Reflectivity contour of a HCG as a function of wavelength and grating thickness simulated by RCWA. The incident wave has a TE polarized, surface-normal incidence, whereas the grating has a duty cycle of 0.7 and a refractive index of 3.48. The mode cutoffs (λ_{c2}, λ_{c3}, etc.) are marked to clearly illustrate the differences of the three wavelength-regimes: deep-subwavelength, near-wavelength and diffraction. (b) Analytical solutions of Fabry-Perot (FP) resonance conditions of the individual modes (Eq. (3), shown by the blue curves, superimposed on the reflectivity contour in 2(a). Excellent agreement is obtained between the analytic and simulation results. Green curves correspond to the in-phase selection-rule, whereas yellow curves correspond to the π-phase selection-rule, Eq. (4). The insets show examples of an anti-crossing and a crossing between the FP resonance lines (blue curves).

For wavelengths longer than λ_{c2}, only one grating mode exists and the grating operates in the deep-subwavelength regime, behaving like a quasi-uniform layer. The reflectivity contour is governed by a simple Fabry-Perot (FP) mechanism, which is recognizable by the (quasi) linear bands in Fig. 2(a). For wavelengths shorter than λ_{c3}, on the other hand, more and more modes emerge, and the reflectivity contour shapes become less and less ordered. Below the subwavelength limit ($\lambda<\Lambda$), the grating enters the *diffraction regime*, where higher diffraction orders emerge outside the grating and reflectivity is greatly reduced.

The intricate "checker-board" contour-shapes of the dual-mode regime in Fig. 2(a) suggest a strong underlying order. To understand it, we must characterize the propagation and evolution of the waveguide-array modes by including the effects of the exiting planes. This involves two additional matrices we should consider. The first matrix is a diagonal propagation matrix $\boldsymbol{\varphi}$ [27], describing the phases accumulated by the modes as they propagate within the gratin from $z = 0$ to $z = t_g$, or vice versa. This is a simple diagonal matrix, given by: $\boldsymbol{\varphi}_{nn} = \exp(-j\beta_n t_g)$, where β_n is the z-wavenumber of nth mode.

The second and most important matrix is the reflection matrix $\boldsymbol{\rho}$. When the modes reach the output plane ($z = t_g$), and subsequently return to the input plane ($z = 0$), due to the abrupt change in refractive index profiles, they **couple into each other** in addition to reflecting back to themselves. This means the off-diagonal coefficients $\boldsymbol{\rho}_{nm}$ ($n \neq m$) are nonzero. A full detailed derivation of $\boldsymbol{\rho}$ is available in Ref. [27]. This is a unique property of HCG, where the orthogonal (waveguide array) modes are coupled at the input and output planes due to an abrupt and large index profile change.

#160825 - $15.00 USD Received 4 Jan 2012; revised 12 Mar 2012; accepted 15 Apr 2012; published 26 Apr 2012
(C) 2012 OSA

In the dual-mode regime, the sizes of **φ** and **ρ** are only 2x2. Let us denote by $2\psi_n$ as the phases accumulated by the waveguide-array modes during one round-trip through the grating. These phases are given by

$$\psi_n \overset{\Delta}{=} \text{phase}\left(\text{eigenvalue } \#n \text{ of } \boldsymbol{\rho\varphi}\right) \tag{2}$$

The Fabry-Perot resonance conditions for phases defined in Eq. (2) are simply

$$\psi_n = m\pi, \text{ where } m = 1, 2, ... \tag{3}$$

Next, the **analytical solutions** of Eq. (3) are plotted on top of the simulated reflectivity contour plots for comparison, shown as the blue solid lines in Fig. 2(b). The blue solid lines appear to follow two families of curves. The first set are nearly linear, corresponding to the first mode: $\psi_1 = m\pi$, whereas the second set are nearly parabolic, corresponding to the second mode: $\psi_2 = m\pi$. If we follow one blue curve, we can pass continuously form a mode of the first kind (linear curve) to a mode of the second kind (parabolic curve), or vice versa. Coupling of the two waveguide array modes are clearly observed. An excellent agreement is obtained between the analytical FP resonance lines and the simulated reflectivity contour testifying to the fact that the physics of HCG features resides in Eq. (3).

The *intersection* points of the blue grid lines correspond to

$$\left|\Delta\psi\right| = \left|\psi_2 - \psi_1\right| = l\pi, \quad \text{where} l = 0, 1, 2, \ldots \tag{4}$$

The intersection of the two grid lines indicates that both modes reach their Fabry-Perot conditions *simultaneously*. When the two FP lines have an odd number multiple of π-phase difference (odd *l*), the blue grid-lines simply cross each other, herein referred to as "crossing". On the other hand, when the intersecting FP lines are in-phase, (even *l*), the two FP lines repel against each other, forming an "anti-crossing". The detailed views of these intersections are shown at the two right insets of Fig. 2(b). Notably, near the anti-crossing point, the reflectivity changes drastically with wavelength and thickness. The crossing can be understood as follows. When the two modes arrive to the output plane ($z = t_g$) with a *π-phase difference* (odd *l*), they *interfere destructively, thus cancelling out the transmission*, and causing the power to be reflected. The "cancelation" of transmission refers to cancellation of the coupling to the 0th order diffraction. Since HCG has subwavelength period in the exiting medium, only the 0th order diffraction carries energy. When there is no transmission into the 0th order diffraction, full reflection is obtained. More of this mechanism can be found in [27]. An anti-crossing happens when the two modes arrive *in-phase* (even *l*) and interfere constructively, resulting in a resonance built-up inside the grating. The resonance manifests itself as a sharp change in reflection over a small span of wavelength [28].

Next, we plot family curves of single-trip phase differences between the two modes. We note that all high reflectivity "checker boxes" are connected by odd *l* curves (depicted by green curves), whereas the low reflectivity boxes are connected by even ones (depicted by yellow curves). By adjusting HCG duty cycle, refractive indices and incident beam polarization, the curves can be shifted and optimized. These set of lines help to guide the optimization process.

4. Crossings and anti-crossing

Figures 3(a) and 3(b) present the intensity profiles in the grating for the cases of an anti-crossing and a crossing, respectively, using the analytical formulation presented here. Anti-crossing corresponds to a very strong resonance, where a very significant (10^7-fold) intensity buildup occurs within the grating. On the other hand, crossing is shown to correspond to a fairly weak (25x) energy buildup. The phenomena of band anti-crossings are commonly observed in physics and, more specifically, optics. Examples include coupled quantum-dot

#160825 - $15.00 USD Received 4 Jan 2012; revised 12 Mar 2012; accepted 15 Apr 2012; published 26 Apr 2012
(C) 2012 OSA

cavities [30,31], semiconductor alloys [32], photonic crystals [33], optical modulators [34], and many others. In all cases, anti-crossings are known to be indicators of strong coupling, while crossings typically indicate weak or no coupling.

Within optics and electromagnetism, crossings and anti-crossings are typically presented in ω-β diagrams, rather than in a t_g-λ diagram, which we chose because the effect can be more clearly seen. However, the two representations are indeed very similar, since as we mentioned above, $\psi_n = m\pi$ are merely generalizations of the simpler condition $t_g = m\pi\beta_n^{-1}$, and therefore the blue grid-lines in Fig. 2(b) is equivalent to a β^{-1}-ω^{-1} diagram. Hence, all intuitions behind crossings and anti-crossings in standard texts apply.

The resonance in Fig. 3(a) is a first order resonance, which is defined as the number of intensity peaks along the *z*-axis at the center of the air gap (in this case $x/\Lambda = 0.15$). This is not incidental: All anti-crossings that are located along the right-most parabolic grid-line (corresponding to $\psi_2 = \pi$) yield first order resonances. Similarly, all anti-crossings that are located along the second rightmost parabolic grid-line ($\psi_2 = 2\pi$) yield second order resonances, etc. In other words, the resonance order is determined by ψ_2.

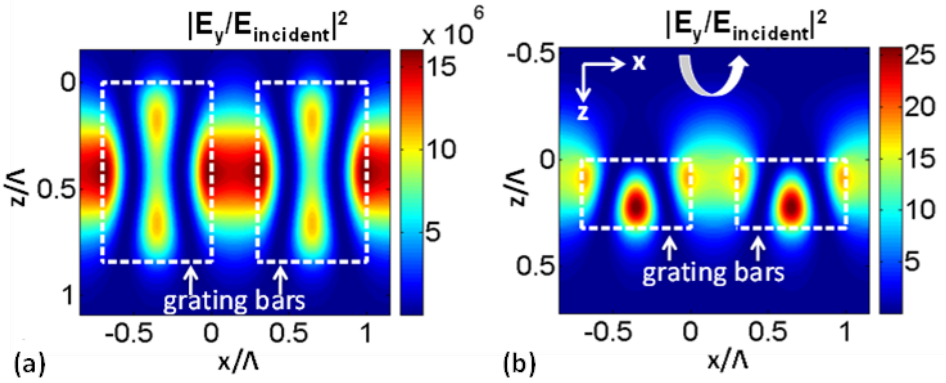

Fig. 3. Intensity profiles inside the grating calculated using analytical formulation presented in this paper for (a) an anti-crossing (same anti-crossing as in the inset of Fig. 2(b)), showing 10^7-fold resonant energy buildup, and (b) a crossing (same as in Fig. 2(b)), showing only weak energy buildup. The parameters are (a) $\lambda/\Lambda = 2.3291$, $tg/\Lambda = 0.8415$, $\eta = 0.70$, $n_r = 3.48$ and (b) $\lambda/\Lambda = 2.02$, $tg/\Lambda = 0.32$, $\eta = 0.70$, $n_r = 3.48$, all with TE-polarization.

The *high-Q* resonance phenomenon in HCG can therefore be explained as merely a result of *strongly coupled simultaneous FP resonances* of two waveguide-array modes. The relation between strength of coupling and ψ_n is straightforward: When the intersecting grid lines are in-phase, the FP resonances have the same *parity* (both odd, or both even) and their intensity profiles overlap significantly, which leads to strong coupling between them and results in an anti-crossing. In contrast, an opposite parity between the two resonances leads to a weak coupling, resulting in a crossing.

To verify that crossings and anti-crossings are inherent characteristics to an HCG structure, rather than merely a feature of our solution method, we plot in Fig. 4 the reflectivity contour t_g-λ of the same grating with input at a large glancing angle (85°) incidence. The advantage of using a shallow angle is that the reflectivity is high everywhere except for resonance lines, thus making the crossings and the anti-crossings clearly visible directly from the reflectivity contour, without any need for us to overlay derivations from Eq. (3) on top of the figure. Of course, one should also note that due to the shallow incidence angle, the propagation constants β_n are different from those of surface normal incidence. Hence Figs. 4 and 2 show different FP lines, despite of the same physical dimensions.

#160825 - $15.00 USD Received 4 Jan 2012; revised 12 Mar 2012; accepted 15 Apr 2012; published 26 Apr 2012
(C) 2012 OSA

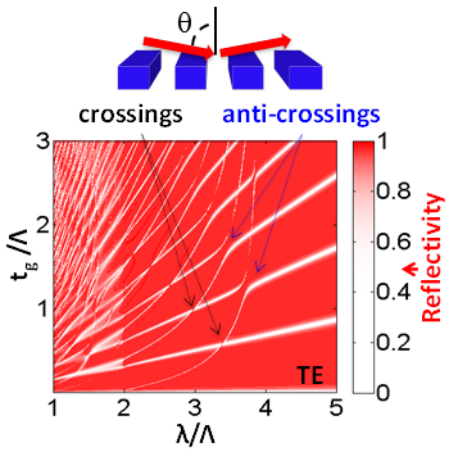

Fig. 4. Reflectivity contour for the same HCG as in Fig. 2 but with a shallow angle (θ = 85°) incidence. The crossings and anti-crossings are clearly seen.

5. Conclusion

In conclusion, we introduce simple and intuitive relations between the phases of the grating modes, which explain completely the extraordinary features of HCG. We believe the analytical formulation and phase selection rules presented here can be very useful in design optimization of HCG reflector or resonator. Given a certain material combinations limited by device specifics, one can determine the dual-mode region, $\lambda_{c2} < \lambda < \lambda_{c3}$, using the analytic formula. One can then create the FP lines in a t_g-λ plot (both normalized by the grating period) and locate the crossings and the anti-crossings, based on Eqs. (3) and (4). For a very broadband reflector, it is necessary to choose a duty cycle that yields a wide spectral spacing between the parabolic grid lines. On the other hand, for a high-Q resonator, it is necessary to choose a duty cycle which leads to a large anti-crossing gap (i.e. large resonant coupling) at the lowest first order resonance, since the lowest (i.e. smallest t_g) first order resonance typically has the highest Q. We expect that the theoretical foundation laid in this work will help to harness the enormous potential of near-wavelength gratings.

Acknowledgments

The authors wish to acknowledge the support of U.S. Department of Defense National Security Science and Engineering Faculty Fellowship N00244-09-1-0013, National Science Foundation (NSF) grants EEC-0812072 and ECCS-1002160, as well as the National Natural Science Foundation of China (NSFC) under grant 61071084, and the State Key Laboratory of Advanced Optical Communication Systems and Networks, China.

#160825 - $15.00 USD Received 4 Jan 2012; revised 12 Mar 2012; accepted 15 Apr 2012; published 26 Apr 2012
(C) 2012 OSA